Draft version February 2, 2022
Typeset using LaTeX default style in AASTeX62

PROPERTIES OF THE INTERSTELLAR MEDIUM ALONG SIGHT LINES TO NEARBY PLANET-HOSTING STARS*

Eric Edelman,[1,2] Seth Redfield,[1] Jeffrey L. Linsky,[3] Brian E. Wood,[4] and Hans Müller[5]

[1]*Department of Astronomy and Van Vleck Observatory, Wesleyan University, Middletown, CT 06459, USA*
[2]*Department of Physics and Astronomy, Embry-Riddle Aeronautical University, Prescott, Arizona 86301, USA*
[3]*JILA, University of Colorado and NIST, Boulder, CO 80309-0440, USA*
[4]*Naval Research Laboratory, Space Science Division, Washington, DC 20375, USA*
[5]*Department of Physics and Astronomy, Dartmouth College, Hanover, NH 03755, USA*

ABSTRACT

We analyze high-resolution ultraviolet spectra of three nearby exoplanet host stars (HD 192310, HD 9826, and HD 206860) to study interstellar properties along their lines of sight and to search for the presence of astrospheric absorption. Using *HST*/STIS spectra of the Lyman-α, Mg II, and Fe II lines, we identify three interstellar velocity components in the lines of sight to each star. We can reliably assign eight of the nine components to partially ionized clouds found by Redfield & Linsky (2008) on the basis of the star's location in Galactic coordinates and agreement of measured radial velocities with velocities predicted from the cloud velocity vectors. None of the stars show blue-shifted absorption indicative of an astrosphere, implying that the stars are in regions of ionized interstellar gas. Coupling astrospheric and local interstellar medium measurements is necessary to evaluate the host star electromagnetic and particle flux, which have profound impacts on the atmospheres of their orbiting planets. We present a table of all known exoplanets located within 20 pc of the Sun listing their interstellar properties and velocities predicted from the local cloud velocity vectors.

Keywords: Galaxy: local interstellar matter — ISM: clouds — ISM: kinematics and dynamics — stars: mass loss — Line: profiles — Techniques: spectroscopic

1. INTRODUCTION

Ultraviolet spectra of nearby late-type stars are imprinted with unique information from several distinct regions along the line of sight: (a) emission lines and continua from the star's chromosphere and higher temperature regions, (b) astrospheric Lyman-α absorption controlled by the stellar mass loss rate, (c) the absorption by interstellar gas superimposed on the stellar emission lines, and (d) heliospheric Lyman-α absorption controlled by the solar mass loss rate. The resulting complexity in the Lyman-α profile mirrors the complexity of the interaction of stars with their surrounding interstellar environments. This interface can be detected for nearby stars. Equipped with stellar wind models and measurements of the local interstellar medium (LISM), these detections can be used to estimate the relatively modest stellar winds of solar-type stars. These winds are only modest in the context of the winds of evolved stars, and can have a profound influence on the evolution of planetary atmospheres in the system.

The *Hubble Space Telescope* (*HST*), in particular with use of its Space Telescope Imaging Spectrograph (STIS) and Cosmic Origins Spectrograph (COS) instruments, is providing invaluable ultraviolet (UV) spectra critical for studying the interactions between stars, their planets, and the LISM. The stellar electromagnetic flux, in particular the UV flux, which can dominate the photochemistry and structure of planetary atmospheres (Miguel et al. 2015), has been evaluated in the context of exoplanets for solar-type stars of different ages (Linsky et al. 2012) and M-dwarf stars (France et al. 2016). Lyman-α, the largest contributor of UV photons for late-type stars has been studied in detail by

eedelman@wesleyan.edu

sredfield@wesleyan.edu

* Based on observations made with the NASA/ESA Hubble Space Telescope obtained from the Data Archive at the Space Telescope Science Institute, which is operated by the Association of Universities for Research in Astronomy, Inc., under NASA contract NAS AR-09525.01A. These observations are associated with programs #12475, 12596.

Wood et al. (2005b) and Youngblood et al. (2016). Measurements of the intervening local interstellar medium (LISM) properties are necessary in order to reconstruct the intrinsic stellar Lyman-α line.

A spectral signature in Lyman-α also results from the interaction between outflowing stellar wind protons with neutral hydrogen from the interstellar cloud in which the star is embedded. As described in the now standard heliospheric model (e.g., Zank et al. 2009), the supersonic stellar wind first decelerates in a termination shock, then flows outward and around the star in a subsonic flow ending at the astropause. Pristine interstellar gas is located farther from the star beyond either the bow shock (Izmodenov et al. 2003; Scherer, & Fichtner 2014) or bow wave (McComas et al. 2012). Measurements of this particle flux from stars is of prime importance when investigating the evolution of planetary atmospheres. For example, Lammer et al. (2013) have argued that Mars lost much of its atmosphere from sputtering when its global magnetic field weakened once the planetary core cooled. The astrospheric technique for measuring mass-loss rates from nearby late-type stars is described by Wood et al. (2004).

The *Voyager 1* and *Voyager 2* spacecraft provided a clear test of the heliospheric model when they crossed the solar termination shock in 2004 (Stone et al. 2005) and 2007 (Stone et al. 2008), respectively, and have provided direct measurements of the plasma pressure and magnetic field strength in the inner heliosheath region inside the heliopause as a function of distance from the Sun (Decker et al. 2008). Information from the *Voyagers* and other spacecraft, such as *Ulysses*, have provided realistic tests of MHD and kinematic models of the heliosphere that focus on the interaction between the solar plasma and LISM neutrals (e.g., Wood 2004). The *Voyager* spacecraft continue to make measurements in regions that are more and more dominated by the LISM, with Voyager 1 believed to have crossed the heliopause in August of 2012 (Gurnett et al. 2013), while Voyager 2's crossing occurred more recently during November of 2018. Zachary et al. (2018) present *HST* observations of nearby stars along the *Voyager 1* and *Voyager 2* sight lines to compare *in situ* measurements of the local plasma with spectroscopic measurements of LISM absorption. Given the ubiquity of stellar winds and surrounding interstellar material, these models can be generalized and applied to other stars. By changing a few essential parameters, heliospheric models can be used to characterize the analogous structures around other stars, called astrospheres.

Within an astrosphere, the astropause is the site of charge exchange between ISM plasma and the inflowing ISM neutrals, with the neutral H I from the ISM giving up an electron to a proton to create a population of very hot neutral hydrogen known as the "hydrogen wall". The hydrogen wall is centered near 150 AU for the Sun, but it can reside at different distances from stars depending on the stellar mass-loss rate and the relative velocity of the star compared to the interstellar flow (Müller et al. 2006). This relatively dense neutral hydrogen, which has been decelerated relative to the interstellar gas flow, produces broad Lyman-α absorption that is redshifted relative to the interstellar gas flow as seen from the star (e.g., the heliosphere) but blueshifted as seen from an external perspective (e.g., astrospheres).

With high-resolution spectra, it is possible to disentangle the astrospheric and heliospheric absorption features from the LISM absorption in the Lyman-α line and thereby characterize the LISM along the line of sight to a nearby star. The column density (N(H I)) of an astrospheric absorption feature depends on the astrosphere size and density enhancement in the hydrogen wall, which is proportional to the strength of the stellar wind. Therefore, a measurement of the astrospheric N(H I) can be used to measure the mass flux of a stellar wind (Wood et al. 2004), which is an important variable to consider when analyzing the evolution of planetary atmospheres and ultimately the habitability of the planets. This is the only observationally based technique presently available for obtaining mass-loss rates for solar-like and cooler stars (Wood et al. 2014b).

A large stellar wind could strip an otherwise habitable planet of its atmosphere. It is likely that Mars lost its atmosphere in this fashion 4 billion years ago by a more active, younger Sun (Wood et al. 2004; Lammer et al. 2013). Moreover, in situ measurements from *MAVEN* provide insights into the rates of atmospheric loss of present day Mars due, in large part, to solar influences (Jakosky et al. 2018), which, alongside evidence of Venus' atmospheric loss due to solar wind interactions in the form of its tail ray detection (Grünwaldt et al. 1997) show that stellar mass-loss rates for a given star can be intimately tied to the atmospheric evolution of their planets. Obtaining wind-strength measurements for more solar-like stars at different points in their life span can provide the data needed to model the interactions between solar/stellar winds and planetary atmospheres through the history of the solar system and other planetary systems.

Understanding the structure and kinematics of interstellar gas in the local region of space has long been important to study general interstellar phenomena (Frisch, Redfield, & Slavin 2011). The local interstellar medium (LISM) plays an important role in this study, because local interstellar gas can be more easily studied along the less complex short sight lines. The reduction in absorption profile confusion due to line blending allows the complexities of the

LISM (e.g., abundances, dynamics, turbulence, etc.) to be studied in great detail. In order to measure nearby stellar winds using the Lyman-α line, knowledge of the LISM is essential for accurately modeling the intrinsic stellar Lyman-α profile. We must also know the LISM flow vector (speed and direction) relative to a star, in order to determine the three-dimensional orientation of the nose of the astrosphere and to estimate stellar wind properties from the astrospheric absorption (Wood et al. 2004). Finally, interstellar absorption decreases the detected flux in emission lines, in particular Lyman-α. Wood et al. (2005b) and Youngblood et al. (2016) found that absorption by interstellar H I reduces the observed flux of even nearby stars by factors of 3–10. This is important because Lyman-α is the brightest emission line in the UV spectrum of solar type stars, and the intrinsic Lyman-α flux is nearly as large as the entire UV spectra of M dwarf stars (France et al. 2012). Knowledge of the column density and velocity structure of interstellar gas in the line of sight to a star is needed to reconstruct stellar Lyman-α fluxes (Wood et al. 2005b; Linsky et al. 2013; Youngblood et al. 2016). The intrinsic Lyman-α flux has an important influence on the photochemistry of exoplanetary atmospheres (Miguel et al. 2015).

Redfield & Linsky (2008) have proposed a model of the LISM consisting of 15 partially ionized clouds located within 15 pc in an otherwise ionized medium. Their model is based on high-resolution spectra of interstellar absorption lines seen against stellar Lyman-α, Mg II, Fe II, and other UV emission lines. The spectra of 157 stars observed with STIS and the earlier Goddard High Resolution Spectrograph (GHRS) on *HST* provide radial velocities and column densities for interstellar matter along these sight lines. They found that the radial velocities measured in sight lines extending over a wide angle in Galactic coordinates are consistent with velocity vectors for these regions that define the two-dimensional structure of 15 clouds. While some sight lines have only a single interstellar radial velocity indicating a single cloud in this line of sight, many stars located within a few parsecs show 2–4 velocity components indicating several clouds along the line of sight. However, individual sight line observations cannot constrain where along the sightline the clouds are located or whether the star at the end of the sightline is beyond or embedded within one of the clouds. Redfield & Linsky (2015) confirm that a model of 15 bulk flow clouds is a more accurate characterization of the LISM than a small number of kinematically deformed clouds (Gry & Jenkins 2014).

In this paper we analyze STIS high-resolution spectra of three nearby stars that are known to have exoplanets. In Section 2 we describe the observations and our data analysis techniques. In Section 3 we evaluate the properties of LISM clouds detected in the sight lines to these stars. In Section 4 we summarize the known interstellar properties or predict these properties for all known exoplanet host stars within 20 pc. Finally, in Section 5 we evaluate whether the target stars show astrospheric absorption.

2. OBSERVATIONS AND DATA ANALYSIS

2.1. *Observations*

We obtained high-resolution STIS spectra of the exoplanet-host stars HD 9826, HD 192310, and HD 206860. HD 9826 and HD 192310 were observed as a part of *HST* program 12475 "Cool star winds and the evolution of exoplanetary atmospheres" (S. Redfield PI). HD 206860 was observed as part of *HST* program 12596 "In search of a young solar wind" (B. Wood PI). Table 1 lists information on the three target stars. The stars HD 35296 and HD 72905 were also observed with program 12596 and have been analyzed by Wood et al. (2014a), Malamut et al. (2014), and Wood et al. (2014b).

We observed the Mg II 2796.3553 Å and 2803.5324 Å lines and the Fe II 2586.6500 Å and 2600.1729 Å lines with the STIS E230H grating (Hernandez et al. 2011), which covered 2568–2845 Å at high resolving power, $\lambda/\Delta\lambda = 114000$. The Mg II and Fe II lines for HD 192310 are shown in Figure 1. The Mg II lines have a very high signal-to-noise (S/N), but the Fe II lines have a much lower S/N. We observed the deuterium (D I) fine structure doublet at 1215.3376 Å and 1215.3430 Å and the H I Lyman-α doublet at 1215.6682 Å and 1215.6736 Å with STIS grating E140M, which covered 1144–1729 Å at medium resolution, $\lambda/\Delta\lambda = 45800$. A sample of these lines is also shown in Figure 1. Note that the D I doublet is entirely included within the stellar Lyman-α emission line.

2.2. *Fitting the Mg II and Fe II LISM Absorption Lines*

We began our analysis of the interstellar absorption lines of Mg II and Fe II using the *Hubble*-specific data reduction software package known as `CALSTIS` (Lindler 1999) including the data analysis procedures developed for the StarCAT catalog of *HST* stellar spectra (Ayres 2010). The software package performs dark frame subtraction, flat field calibration, flux unit and heliocentric rest frame conversions, wavelength calibrations, and 2-D to 1-D spectrum extraction (Hernandez et al. 2011). Input data to our line profile fitting program includes the atomic parameters of each elemen-

Table 1. Target Star Information.

Object Name	Distance (pc)	l (deg)	b (deg)	Spectral Type	V (mag)	V_R (km s^{-1})	Known Planets
HD 192310	8.91 ± 0.02	15.6	−29.4	K2 V	5.7	-54.2 ± 0.90	2[a]
HD 9826	13.49 ± 0.03	132.0	−20.7	F9 V	4.1	-28.59 ± 0.08	4[b]
HD 206860	17.90 ± 0.14	69.9	−28.3	G0 V	6.0	-16.68 ± 0.09	1[c]

NOTE—All values are taken from the SIMBAD website unless otherwise noted.

[a] Howard et al. (2011), Pepe et al. (2011).

[b] Butler et al. (1997), Butler et al. (1999), Curiel et al. (2011).

[c] Luhman et al. (2007).

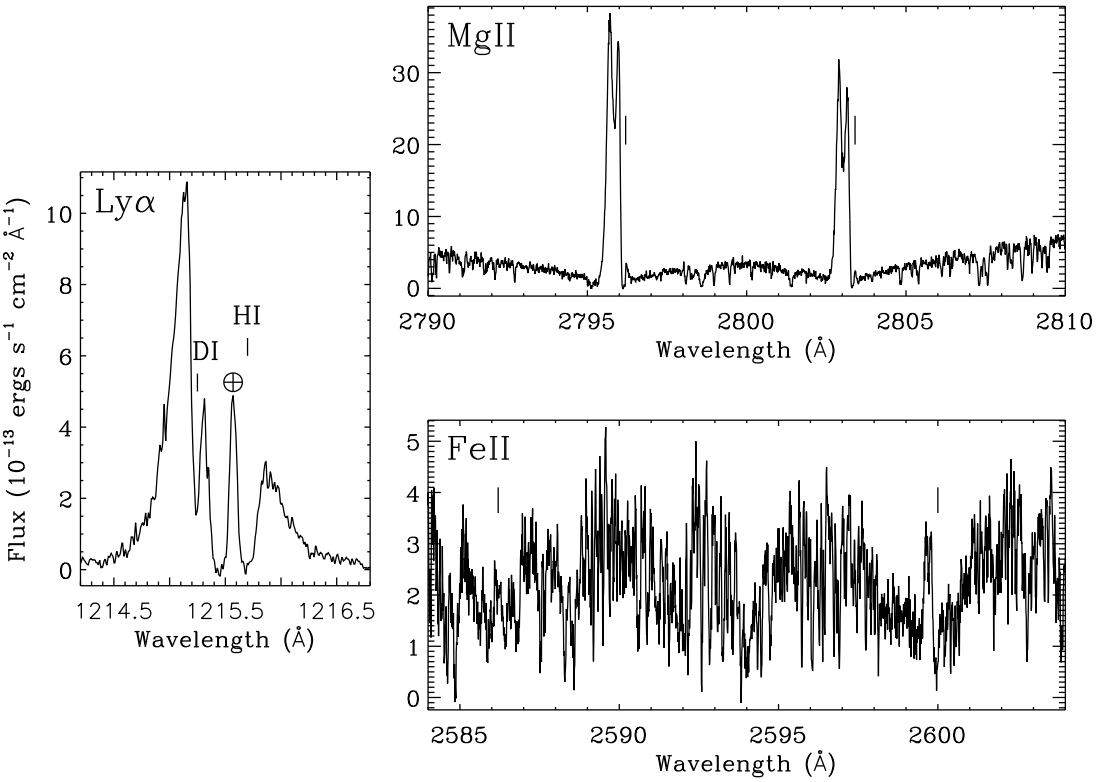

Figure 1. *Left:* STIS Spectrum of HD 192310 showing the stellar Lyman-α emission line of H I and interstellar absorption by H I and D I. Vertical lines mark the center of interstellar absorption by velocity component 1 and the $\oplus$ symbol marks the wavelength of the feature dominated by geocoronal emission, but which also includes a weaker contribution from the solar wind backscattered emission inseparable from the geocoronal emission in this data set. This feature is subtracted from the data prior to analysis due to its position within the portion of the line saturated due to LISM absorption. *Upper right:* The spectrum of the stellar Mg II emission lines at 2796 Å and 2803 Å. The vertical lines indicate absorption by interstellar component 1. *Lower right:* The STIS spectrum of the Fe II 2586 Å and 2600 Å lines with interstellar absorption component 1 marked.

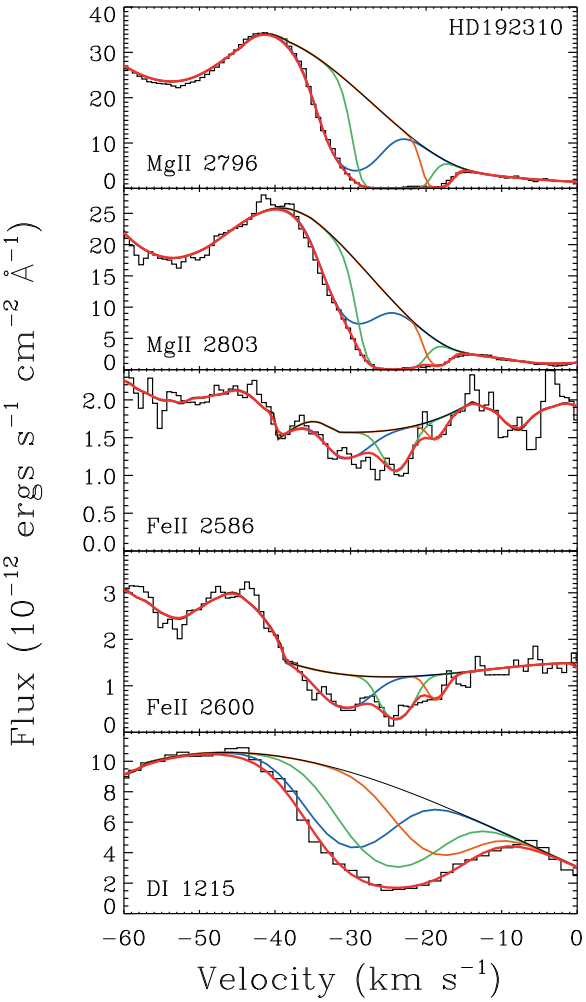

Figure 2. Reconstructed stellar emission lines and interstellar Mg II, Fe II, and D I absorption profiles for the line of sight to HD 192310. The blue (component 1), green (component 2), and orange (component 3) lines represent the individual interstellar absorption, while the red line represents the cumulative absorption by all components convolved with the instrumental line spread function. D I is comprised of two closely spaced transitions (1215.3376 Å and 1215.3430 Å) and modeled as such, but combined and displayed as a single absorption for each component in the figure for clarity.

tal transition taken from Morton (2004) and our initial estimates of the Voigt profile parameters of each absorption feature. With these inputs and information regarding the flux and error for each pixel in the STIS spectrum, we compute the best-fit Voigt profile for each absorption component to obtain the radial velocity of the interstellar gas relative to the Sun, the Doppler width of the line, and its column density. The errors for each parameter are computed through Monte Carlo iterations.

As is shown in Figures 2–4, the absorption profiles of the two Mg II and two Fe II lines are aligned at the same velocity relative to each other. This is expected because these absorption lines are produced by gas in the same cloud or clouds along the line of sight. Table 2 lists the measured radial velocities, Doppler widths, column densities, and S/N for the three absorption components observed in the spectra of each star. These absorption components emerged as the smallest number that could reasonably fit the feature, justified by computing an F-test for each fit with an added component. The agreement of radial velocities measured from the different ions for each interstellar component mostly lie within the 1.5 km s^{-1} velocity precision of STIS.

2.3. *Fitting the H I and D I Lyman-α Absorption Lines*

We next fitted the interstellar Lyman-α absorption lines of atomic hydrogen and deuterium. This procedure differs somewhat from that used to fit the Mg II and Fe II lines, because interstellar absorption removes the core of the

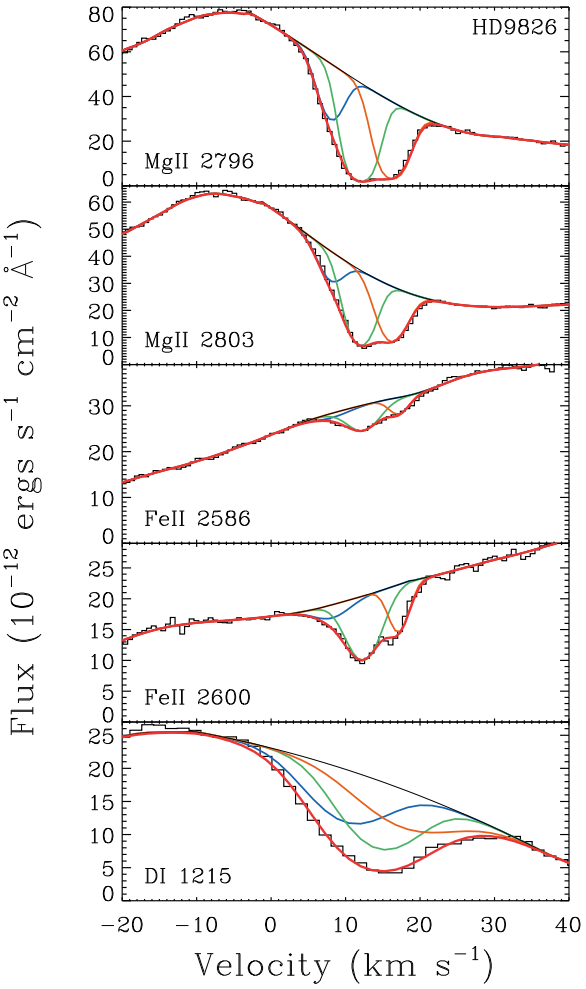

Figure 3. Same as Figure 2 but for HD 9826.

intrinsic stellar Lyman-α emission line, requiring a reconstruction of the intrinsic emission profile. Following the fitting procedure described by Wood et al. (2005, 2014a), we first assume that the absorption velocities of H I and D I are the same and that thermal broadening dominates the width of the H I and D I lines, and therefore differ only due to the factor of two difference in mass. Our fit to the narrow D I line measures the deuterium column density N(D I), which provides an estimate of the hydrogen column density N(H I) given the number density ratio D/H $= 1.56 \times 10^{-5}$ in the LISM (Linsky et al. 2006). This value for N(H I) provides a good estimate of the shape of the intrinsic Lyman-α emission line wings. We also assume that the shape of the Lyman-α line core is similar to that of the Mg II lines including a self-reversal, because both the Mg II and Lyman-α lines are optically thick and are formed in the stellar chromosphere. We then find the best fit to the observed Lyman-α profile by allowing small changes in the intrinsic emission line shape and relaxing the assumption that the H I and D I velocities must be the same. The results of these fits are shown in Figures 5–7 for HD 192310, HD 9826, and HD 206860, and the resulting radial velocities, Doppler widths, and column densities are listed in Table 3.

Since the Lyman-α lines of both H I and D I are fine-structure doublets separated by 0.0054 Å, corresponding to 1.33 km s^{-1}, absorption by each LISM cloud appears as two closely spaced absorption components for each isotope. For all three stars, we find from the Mg II and Fe II absorption spectra that spectra for the sight lines to each star show interstellar absorption at three different velocities. We must, therefore, fit each H I and D I Lyman-α ISM velocity component with three free parameters translating to 12 absorption components. Figures 5–7 show the interstellar absorption profiles for each line of sight, where we combined the closely spaced fine structure lines for clarity. Also shown is the combined line profile convolved with the instrumental line spread function, and the observed spectrum.

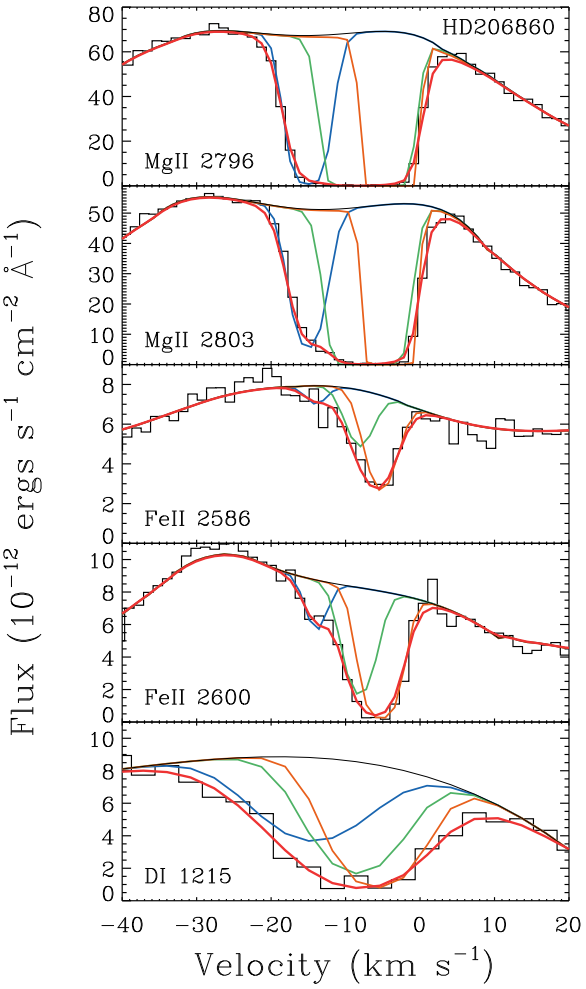

Figure 4. Same as Figure 2 but for HD 206860.

We find satisfactory agreement in the interstellar radial velocity between the line fits of D I/H I and Mg II and Fe II. We conclude, therefore, that interstellar absorption alone without any additional absorption components (e.g., astrospheric or heliospheric absorption) can explain these observations.

3. PROPERTIES OF THE LISM ALONG THE OBSERVED SIGHT LINES

The LISM is a complex environment filled with a variety of partially ionized interstellar gas clouds that produce absorption lines superimposed on the stellar emission line spectra. Ultraviolet resonance lines of H I, D I, O I, C II, Fe II, Mg II, and other atoms and ions are typically observed in high-resolution spectra of even the closest stars (e.g., Redfield & Linsky 2002, 2004). Figures 2–4 show our fits to the major ISM features in the data sets for HD 192310, HD 9826, and HD 206860, respectively. We focus our attention on the high signal-to-noise absorption features of Mg II, Fe II, D I, and of course, H I Lyman-α.

We compare our measurements with the Redfield & Linsky (2008) dynamical model of the LISM. This model uses information gathered from GHRS and STIS observations of 157 sight lines to compute velocity vectors of 15 LISM clouds located within 15 pc of the Sun. For specified Galactic coordinates, the model predicts which clouds intersect or lie within 20° of the sightline to the star, and the radial velocities for these clouds (Redfield & Linsky 2008)[1]. In Table 4 we list the interstellar clouds that best match the three velocity components for each line of sight. We select the most likely clouds on the basis that (1) the line of sight is inside, at the edge, or close to the edge of a known cloud, and (2) the radial velocity predicted from the cloud's velocity vector lies within 2.0 km s^{-1} of the weighted

[1] The LISM Kinematic Calculator: http://lism.wesleyan.edu/LISMdynamics.html

Table 2. LISM Fit Parameters.

Star Name	Component Number	Ion	Radial Velocity (km s^{-1})	Doppler Width (km s^{-1})	Column Density (log N(ion))	S/N
HD 192310	1	Fe II	-30.69 ± 0.66	4.02 ± 0.72	12.57 ± 0.07	5.4
	1	Mg II	-31.1 ± 1.5	3.73 ± 0.82	12.20 ± 0.09	18.2
	1	C II	-29.77 ± 0.87	6.0 ± 1.8	13.46 ± 0.16	2.0
	1	D I	-30.3 ± 1.0	7.0 ± 1.3	12.85 ± 0.20	12.6
	2	Fe II	-24.04 ± 0.51	2.53 ± 0.64	12.57 ± 0.11	5.4
	2	Mg II	-24.46 ± 0.55	3.76 ± 0.60	13.20 ± 0.13	18.2
	2	C II	-23.76 ± 0.87	2.4 ± 1.0	15.15 ± 0.44	2.0
	2	D I	-24.9 ± 1.0	7.7 ± 1.1	13.01 ± 0.13	12.6
	3	Fe II	-19.0 ± 2.1	2.5 ± 1.9	12.10 ± 0.16	5.4
	3	Mg II	-18.9 ± 1.4	2.44 ± 0.76	12.46 ± 0.21	18.2
	3	C II	-18.77 ± 0.87	5.26 ± 0.72	13.64 ± 0.46	2.0
	3	D I	-19.0 ± 1.0	6.6 ± 1.4	12.73 ± 0.23	12.6
HD 9826	1	Fe II	10.9 ± 1.8	3.38 ± 0.63	11.92 ± 0.11	21.1
	1	Mg II	8.05 ± 0.72	2.02 ± 0.29	11.57 ± 0.13	28.2
	1	O I	9.6 ± 1.2	4.61 ± 0.59	13.56 ± 0.19	7.5
	1	D I	10.05 ± 0.90	7.2 ± 1.3	12.69 ± 0.18	19.8
	2	Fe II	12.35 ± 0.86	2.6 ± 1.1	12.19 ± 0.06	21.1
	2	Mg II	12.04 ± 0.16	2.40 ± 0.37	12.49 ± 0.05	28.2
	2	O I	13.6 ± 1.2	2.4 ± 1.1	13.57 ± 0.60	7.5
	2	D I	14.33 ± 0.90	6.7 ± 1.5	12.88 ± 0.16	19.8
	3	Fe II	16.67 ± 0.79	2.04 ± 0.71	12.02 ± 0.09	21.1
	3	Mg II	16.30 ± 0.21	2.47 ± 0.17	12.38 ± 0.05	28.2
	3	O I	17.6 ± 1.2	2.1 ± 1.2	14.5 ± 1.1	7.5
	3	D I	18.24 ± 0.90	8.8 ± 1.9	12.70 ± 0.16	19.8
HD 206860	1	Fe II	-13.80 ± 0.98	2.35 ± 0.71	11.99 ± 0.09	11.4
	1	Mg II	-14.77 ± 0.41	2.59 ± 0.17	12.67 ± 0.04	30.3
	1	D I	-14.84 ± 0.67	9.7 ± 1.6	13.05 ± 0.13	10.4
	2	Fe II	-7.14 ± 0.91	2.47 ± 0.39	12.69 ± 0.12	11.4
	2	Mg II	-7.43 ± 0.69	3.47 ± 0.27	13.22 ± 0.28	30.3
	2	D I	-9.00 ± 0.67	7.1 ± 1.9	13.19 ± 0.38	10.4
	3	Fe II	-5.00 ± 0.65	2.11 ± 0.51	12.89 ± 0.08	11.4
	3	Mg II	-4.87 ± 0.82	2.07 ± 0.30	14.16 ± 0.20	30.3
	3	D I	-6.29 ± 0.67	6.5 ± 1.5	13.31 ± 0.23	10.4

NOTE—S/N based on an average of 10 data points over the emission line near absorption.

mean velocity of the observed narrow interstellar lines (Mg II, Fe II, D I, and either C II or O I). The mean velocities weighted by the inverse square of the measured errors of the individual velocities from Table 2 for each ion are listed in Table 4. Given these criteria, we can reliably match 8 of the 9 velocity components with one or more clouds. In one case (component 1 for HD 206860) there are two plausible cloud identifications, although the line of sight passes outside of the presently known boundaries of both the Vel and Mic clouds. There is no known cloud that matches the line of sight to HD 9826 with a velocity close to that of component 1.

As the measured Doppler width parameter b is equal to the sum of the thermal and non-thermal broadening processes, b can be used to provide reasonable estimations of temperature (T) and turbulence (ξ) of the absorbing gas. This is

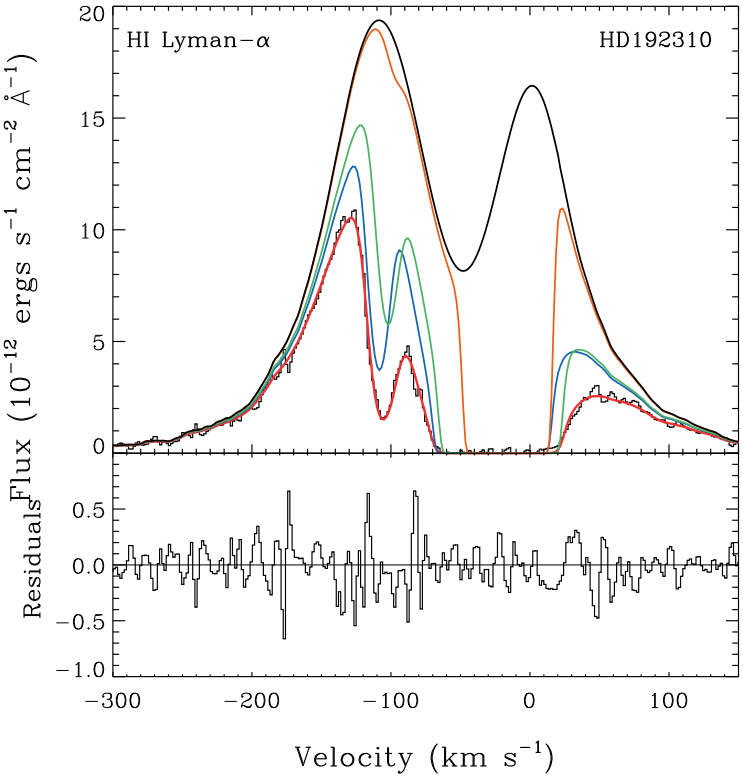

Figure 5. Reconstructed stellar H I Lyman-α emission line (black line) for HD 192310 and interstellar absorption by component 1 (blue line), component 2 (green line), and component 3 (orange line). For each of the three interstellar components there are four absorption lines as the Lyman-α lines of both H I and D I are close doublets. However, for clarity, these have all been combined and displayed as a single absorption feature for each component. The center of D I absorption is at –81.6 km s^{-1} relative to H I. The thick red line is the convolution of the intrinsic Lyman-α emission line with the sum of the interstellar absorption components. It is an excellent fit to the observed profile (thin black histogram). The difference in flux versus the total predicted absorption is plotted in velocity space beneath the fit.

Table 3. Lyman-α ISM Fit Parameters.

Object Name	Component Number	Radial Velocity (km s^{-1})	Doppler Width (km s^{-1})	Column Density (log N(H I))	S/N
HD 192310	1	-27.47 ± 0.45	12.69 ± 0.66	17.96 ± 0.03	8.0
	2	-21.48 ± 0.45	13.45 ± 0.75	17.90 ± 0.03	8.0
	3	-16.47 ± 0.45	11.5 ± 1.4	16.17 ± 0.50	8.0
HD 9826	1	10.83 ± 1.13	13.29 ± 0.30	17.78 ± 0.20	12.2
	2	15.11 ± 1.13	7.53 ± 2.19	17.55 ± 0.17	12.2
	3	19.02 ± 1.13	9.80 ± 1.74	17.34 ± 0.28	12.2
HD 206860	1	-16.6 ± 1.2	10.0 ± 1.5	17.35 ± 0.26	9.7
	2	-10.8 ± 1.2	13.0 ± 1.1	17.79 ± 0.20	9.7
	3	-8.1 ± 1.2	12.0 ± 1.5	18.14 ± 0.17	9.7

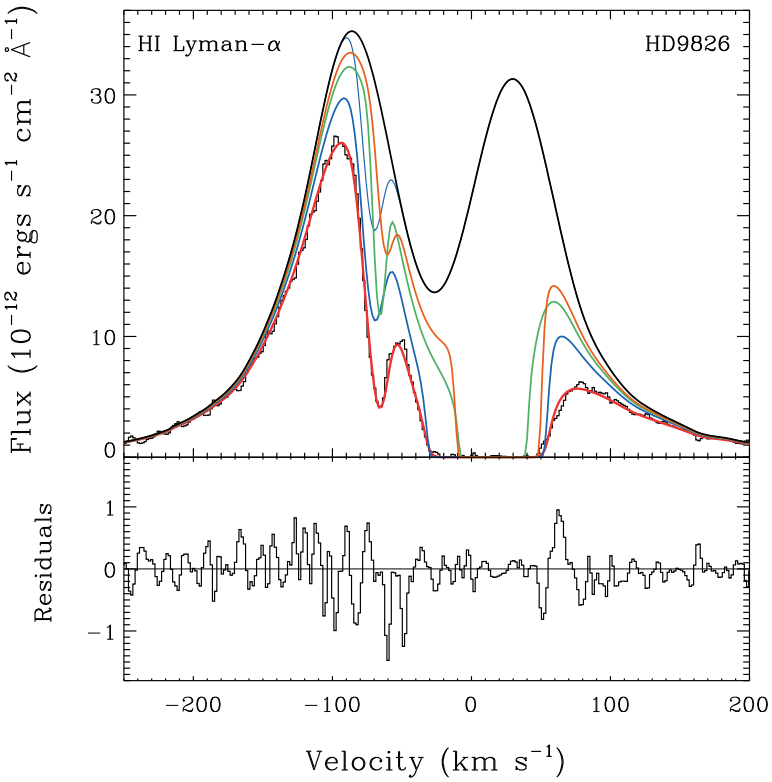

Figure 6. Same as Figure 5 but for HD 9826.

accomplished with the use of the following equation (Draine 2011) that adds together the two broadening factors

$$b^2 = \frac{2kT}{m} + \xi^2, \tag{1}$$

and by taking into account the different ion masses. Figure 8 is an example of such a measurement for component 3 detected toward HD 9826. See Redfield & Linsky (2004) for a more detailed discussion of this technique. In all cases, the agreement of cloud temperature, listed in Redfield & Linsky (2008), with the measured temperature lies within the admittedly large errors, as displayed in Table 4.

We measure the depletions (in log units) for iron and magnesium by comparison with the solar abundances obtained by Asplund et al. (2005), assuming that they are completely in their first ionization state, which is a reasonable assumption (Slavin & Frisch 2008). The values of these properties for the three lines of sight considered in this paper can be found in Table 4, and in most cases are reasonably consistent with the associated cloud averages from Redfield & Linsky (2008). These physical properties of the surrounding interstellar medium (e.g., velocity, temperature, and ionization) become extremely important when creating model astrospheres for stars.

4. PROPERTIES OF THE LISM CLOUDS IN THE SIGHT LINES TO KNOWN PLANET-HOSTING STARS WITHIN 20 PC OF THE SUN

The kinematic and physical properties of the LISM clouds are critical input parameters for analyzing the profiles of stellar emission lines and for measuring the mass-loss rates of host star winds that can erode exoplanet atmospheres. While spectra of Lyman-α and other emission lines obtained during transits provide valuable transmission spectra (e.g., Vidal-Madjar et al. 2003; Fossati et al. 2010; Ehrenreich et al. 2015; Loyd et al. 2017) that can be used to measure the extent and composition of exoplanet atmospheres, interstellar absorption in the line cores severely complicates the analysis. It is essential, therefore, to know and remove the interstellar absorption components in these lines. Spectroscopic follow-up using ground-based telescopes, *HST*, and the *James Webb Space Telescope* of bright

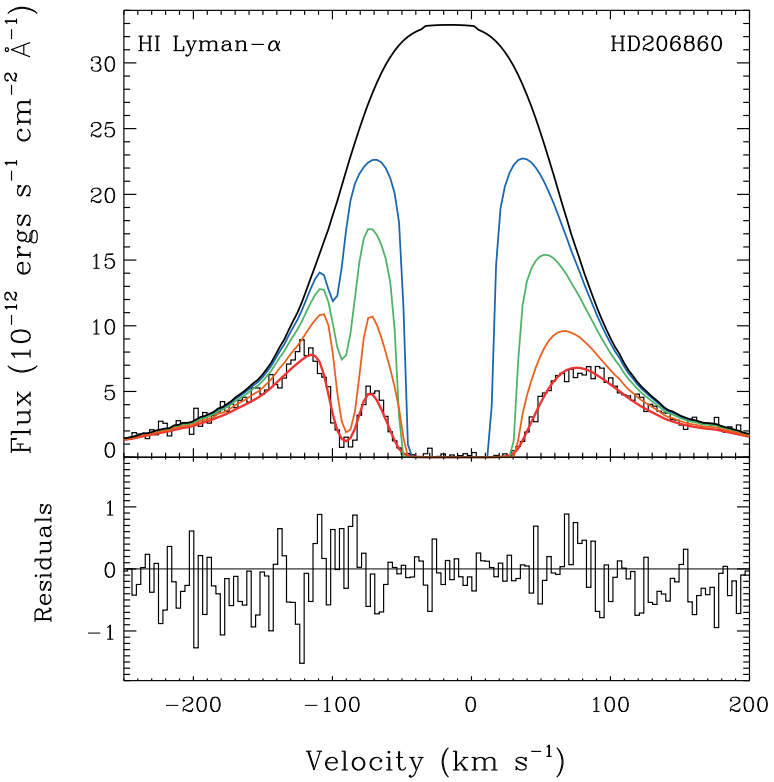

Figure 7. Same as Figure 5 but for HD 206860.

nearby stars with transiting exoplanets discovered by ground and space-based facilities, including the recently launched *Transiting Exoplanet Survey Satellite* (*TESS*) mission will result in powerful studies of exoplanetary atmospheres. To facilitate such studies, we include in Table 6 a summary of the measured and predicted LISM properties for the lines of sight to all presently known exoplanet host stars located within 20 pc of the Sun. This currently totals 96 systems, eight of which contain transiting exoplanets. We compiled the list from the Confirmed Planets Table at the NASA Exoplanet Archive[2] supplemented by Gaia DR2[3] (Gaia Collaboration et al. 2016, 2018) and SIMBAD[4]. We list the measured radial velocities and *log*(H I) column densities for each identified interstellar velocity component, together with references to the original papers.

There are no measured interstellar properties for most of the stars in the list and therefore we rely on the morphological (Redfield & Linsky 2000) and kinematic (Redfield & Linsky 2008) models of the LISM. The clouds traversed by each line of sight to these stars are those for which the Galactic coordinates are inside of or very close to the cloud boundaries shown in Redfield & Linsky (2008). We compute the predicted cloud velocities from the cloud velocity vectors[5], and for lines of sight through the Local Interstellar Cloud (LIC) we compute the H I column densities from the three-dimensional LIC model (Redfield & Linsky 2000)[6]. The first component is likely the strongest absorber. Note that the predicted velocities for several clouds along the same line of sight are similar in many cases. Therefore, low-resolution spectra for these lines of sight will likely show a blended profile of interstellar absorption.

Because strong emission lines, e.g. H I Lyman-α (1216 Å), O I (1302 Å), C II (1334 Å), and Mg II (2796 Å and 2802 Å), are transitions to the ground state, absorption by interstellar atoms and ions, which are always in their ground states, near line center alters the observed profile in ways that can almost completely obscure or significantly alter the signal produced by the exoplanet. The local region of space (<100 pc) occupied by the LISM, is also the

[2] https://exoplanetarchive.ipac.caltech.edu
[3] https://gea.esac.esa.int/archive/
[4] http://simbad.u-strasbg.fr
[5] http://lism.wesleyan.edu/LISMdynamics.html
[6] http://lism.wesleyan.edu/ColoradoLIC.html

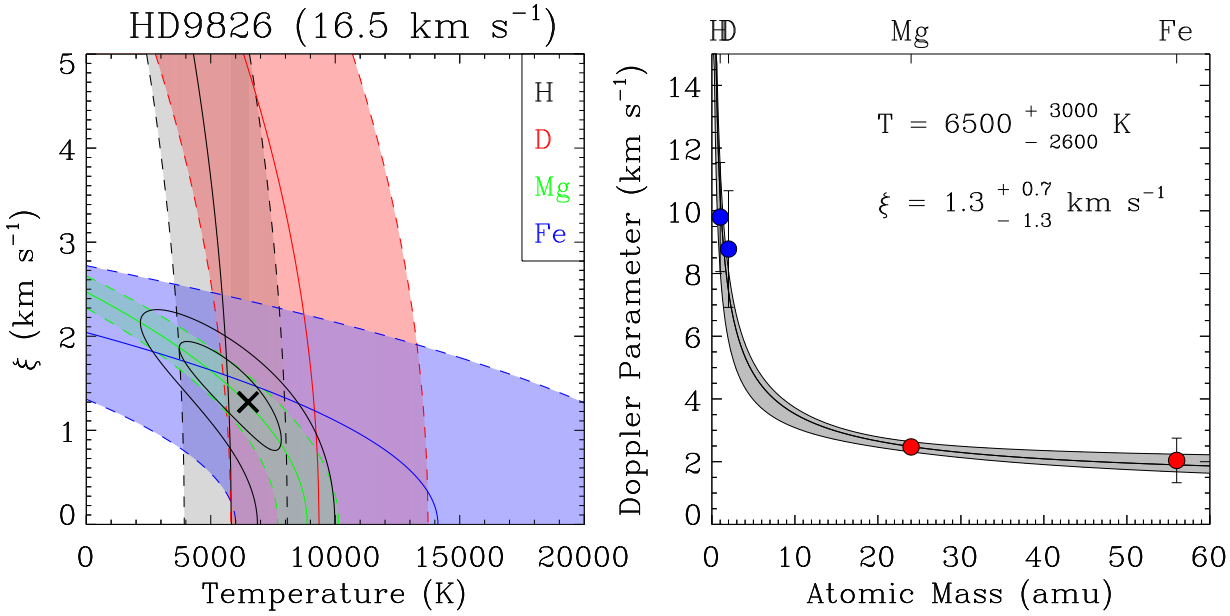

Figure 8. Temperature and turbulent velocity fits for component 3 (≈16.5 km s^{-1} for ions listed in Table 2 and ≈19.0 km s^{-1} for Lyman-α) in the line of sight to HD 9826. *Left:* Solid lines plot the best fit temperature-turbulence relation for H I (black), D I (red), Mg II (green), and Fe II (red) and dashed lines show the 1σ uncertainties in these fits. The × symbol marks the best fit considering all four elements and the curved lines around the × symbol mark the 1σ and 2σ uncertainties. *Right:* Plot of the Doppler width (thermal and turbulent combined) vs. atomic mass for the four elements. The dashed lines above and below the solid line mark the 1σ uncertainty about the mean fit (solid line). The derived uncertainties in the temperature and turbulent velocity are 1σ values.

same volume of the galaxy as the most attractive exoplanets for transmission spectroscopy follow-up. For this reason, it is important to have as complete as possible knowledge on the properties of the LISM.

5. SEARCH FOR SPECTROSCOPIC EVIDENCE OF ASTROSPHERES AND THE HELIOSPHERE

We selected the stars in this study because they are host stars of confirmed exoplanets. The detection of astrospheric absorption from any of the stars would be a great opportunity to infer the mass loss rate from the host star of an exoplanet.

The signature of an astrosphere is additional absorption by H I gas in the star's "hydrogen wall" produced by charge-exchange interactions between the ISM plasma slowed by the outflowing stellar wind and the neutral hydrogen in the interstellar cloud that embeds the star. These interactions lead to Lyman-α absorption that is red-shifted relative to the inflowing gas as seen from the star but blue-shifted as seen by an external observer. We have, therefore, inspected the fitted Lyman-α absorption lines to look for additional absorption on the short wavelength side of the interstellar H I absorption. Figures 5–7 show details of the Lyman-α lines of all three stars, comparing our fit to the observed Lyman-α lines that includes interstellar H I and D I absorption by all 3 velocity components along their sight lines. These figures show no evidence for additional absorption at shorter wavelengths than the interstellar H I absorption and thus no evidence for astrospheric absorption.

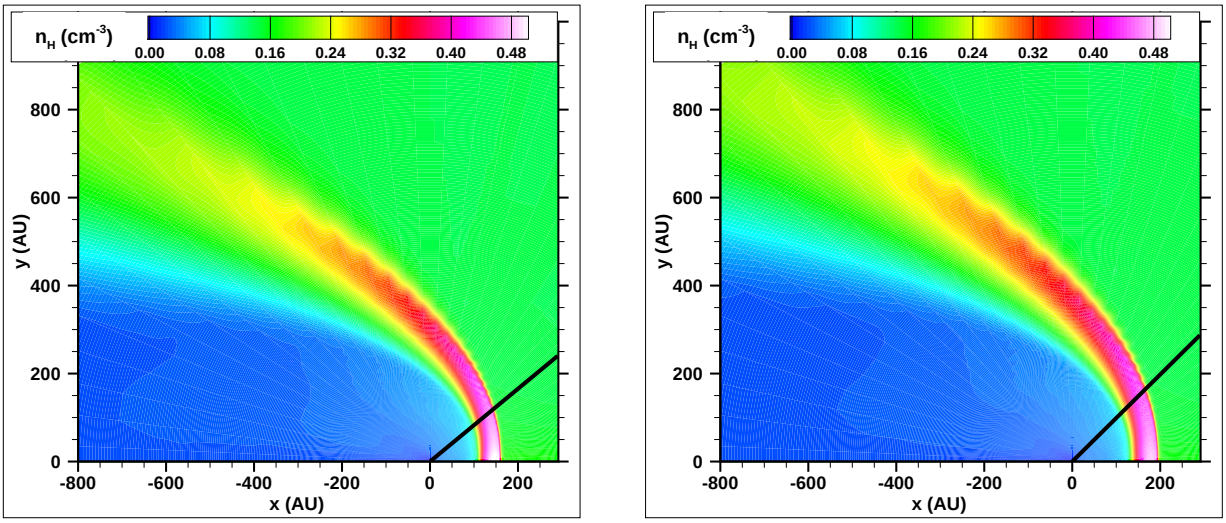

Figure 9. Neutral hydrogen number density distributions surrounding HD 9826 (*left*) and HD192310 (*right*), each located at $x = y = 0$ AU. The LISM flow is coming in from the right. *Left:* density of hot H I surrounding HD 9826, with the line of sight from the Sun to HD 9826 at 39.6° indicated by the black line. The hydrogen wall is clearly seen from the enhancement of the hydrogen density near and trailing from the leading nose of the astrosphere. *Right:* Same for HD 192310, with the line of sight from the Sun to HD 192310 at an angle of 44.7°.

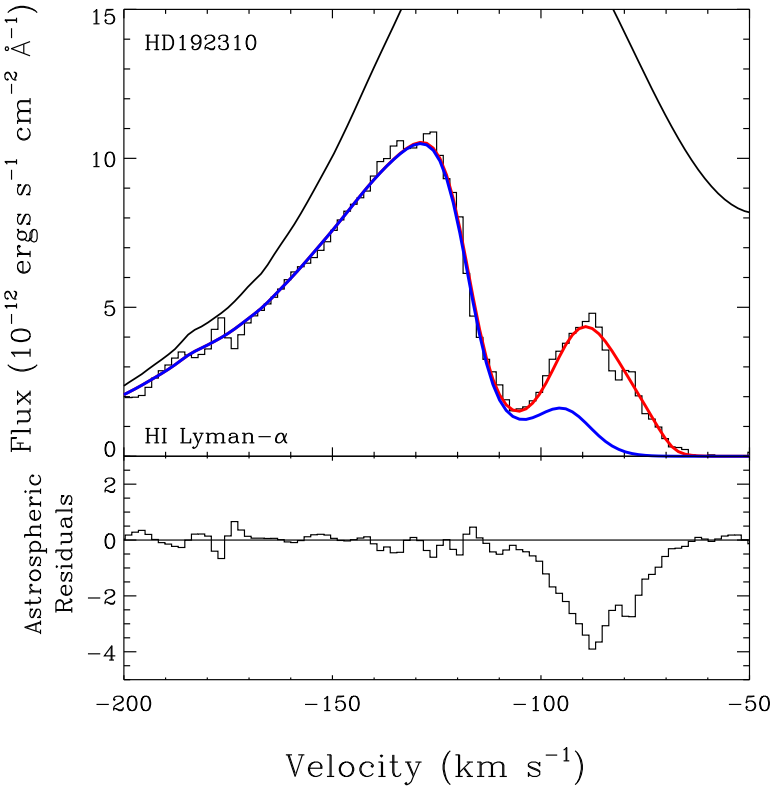

Figure 10. Expanded version of Figure 5 showing the short wavelength side of the reconstructed stellar Lyman-α emission (solid black line) and the observed spectrum (histogram). The red line shows the predicted Lyman-α stellar emission with absorption by the three interstellar components. The blue line shows the effect of including additional absorption from the stellar astrosphere calculated assuming a mass-loss rate of 5.9 $\dot{M}_{\odot}$. Inclusion of this amount of astrosphere absorption produces very large residuals centered at –90 km s^{-1}.

Table 4. Physical Properties of the ISM Towards Planet-Hosting Stars[a]

Star Name	Component or Cloud	v (km s^{-1})	T (K)	ξ (km s^{-1})	D(Mg)	D(Fe)
HD 192310	1	-30.41 ± 0.57	8600^{+2000}_{-1800}	$3.3^{+1.2}_{-1.3}$	-1.29 ± 0.13	-0.84 ± 0.09
	Vel edge	-31.70 ± 1.52	(10600)	(3.5)		(–0.03)
	2	-24.24 ± 0.50	9900^{+2200}_{-2100}	$2.2^{+1.1}_{-2.0}$	-0.23 ± 0.16	-0.78 ± 0.12
	Mic inside	-23.74 ± 1.02	9900 ± 2000	3.1 ± 1.0	-0.03 ± 0.40	-0.92 ± 0.43
	3	-18.88 ± 0.57	6900^{+2600}_{-2300}	$1.3^{+1.6}_{-1.3}$	-0.76 ± 0.55	-0.48 ± 0.53
	LIC outside	-17.32 ± 1.15	7500 ± 1300	1.62 ± 0.75	-0.97 ± 0.23	-1.12 ± 0.10
HD 9826	1	9.1 ± 1.2	10400^{+2000}_{-1900}	$0.00^{+2.4}_{-0.0}$	-1.74 ± 0.25	-1.31 ± 0.23
	unknown					
	2	12.1 ± 1.1	4000^{+2800}_{-2200}	$1.8^{+0.8}_{-1.2}$	-0.59 ± 0.20	-0.81 ± 0.19
	Hyades inside	12.06 ± 1.09	6200 ± 3800	2.7 ± 1.2	-1.06 ± 0.47	-0.32 ± 0.62
	3	16.45 ± 0.88	6500^{+3000}_{-2600}	$1.3^{+0.7}_{-1.3}$	-0.49 ± 0.30	-0.77 ± 0.30
	LIC inside	14.44 ± 1.23	7500 ± 1300	1.62 ± 0.75	-0.97 ± 0.23	-1.12 ± 0.10
HD 206860	1	-14.68 ± 0.58	7100^{+2800}_{-2400}	$1.4^{+0.6}_{-1.4}$	-0.21 ± 0.28	-0.81 ± 0.28
	Vel outside	-15.36 ± 0.99	(10600)	(3.5)		(–0.03)
	Mic outside	-16.33 ± 1.34	9900 ± 2000	3.1 ± 1.0	-0.03 ± 0.40	-0.92 ± 0.43
	2	-8.0 ± 1.0	9600^{+2500}_{-2300}	$2.11^{+0.54}_{-0.68}$	-0.10 ± 0.36	-0.55 ± 0.24
	Eri inside	-8.65 ± 0.99	5300 ± 4000	3.6 ± 1	-0.15 ± 0.30	-0.39 ± 0.19
	3	-5.44 ± 0.79	6800^{+2700}_{-2500}	$0.80^{+0.98}_{-0.80}$	-0.49 ± 0.28	-0.70 ± 0.19
	LIC edge	-6.70 ± 1.35	7500 ± 1300	1.62 ± 0.75	-0.97 ± 0.23	-1.12 ± 0.10

[a] Sight line velocities are the weighted means of the heavy ions measured in Table 2. The errors are the larger of either the error on the weighted mean or the standard deviation of the individual values. The corresponding clouds are indicated by name and whether the sightline is inside, at the edge (i.e., <20°), or well outside (i.e., >20°) of the cloud boundaries identified by Redfield & Linsky (2008). For HD 9826, component 1 corresponds to no known cloud. For HD 206860, component 1 is more likely the Vel Cloud but could be the Mic Cloud. Cloud parameters in parenthesis are based on only one line of sight.

Another test for astrospheric absorption is to compare the relative velocities of interstellar H I and D I absorption. Note that the rest wavelengths for the H I and D I lines automatically include the theoretical wavelength difference of 0.3307 Å, corresponding to 81.6 km s^{-1}. If a star has a hydrogen wall, then the central velocity of H I absorption (produced by interstellar and astrospheric absorption) will be shifted to shorter wavelengths (blueshifted). The velocity difference, $\Delta v = v(\mathrm{H\ I}) - v(\mathrm{D\ I})$, is typically $-3\,\mathrm{km\,s^{-1}}$ (e.g., Wood et al. 1996). On the other hand, if there is no astrospheric absorption and the line of sight traverses the hydrogen wall around the Sun, then the velocity difference will be positive (redshifted) due to the heliospheric absorption, resulting in a $\Delta v \approx 3\,\mathrm{km\,s^{-1}}$. We find that the observed velocity difference average (Δv) for the three interstellar components is 2.93 km s^{-1} for HD 192310, +0.78 km s^{-1} for HD 9826, and –1.79 km s^{-1} for HD 206860. These small velocity differences could be explained by systematic errors in the fitting procedure resulting from the need to simultaneously analyze the three blended components along the line of sight resulting in 12 absorbing columns for each Lyman-α line profile. However, the velocity difference for HD 192310 does approach $3\,\mathrm{km\,s^{-1}}$, and therefore indicates possible heliospheric absorption. Wood et al. (2005b) provides evidence that HD 192310's total $\log N(\mathrm{H\ I})$ value may be low enough for detectable heliosphere absorption, which could warrant further observation and analysis of this sight line.

There are several possible explanations for the absence of a measurable astrospheric absorption signature in the Lyman-α line profiles. If the interstellar hydrogen column density $\log N(\mathrm{H\ I}) > 18.7$, then the very broad Lyman-α absorption would completely absorb the underlying astrospheric absorption. This is not the case for these three sight lines since the sum of the three absorption components does not exceed $\log N(\mathrm{H\ I}) = 18.4$ for any sight line.

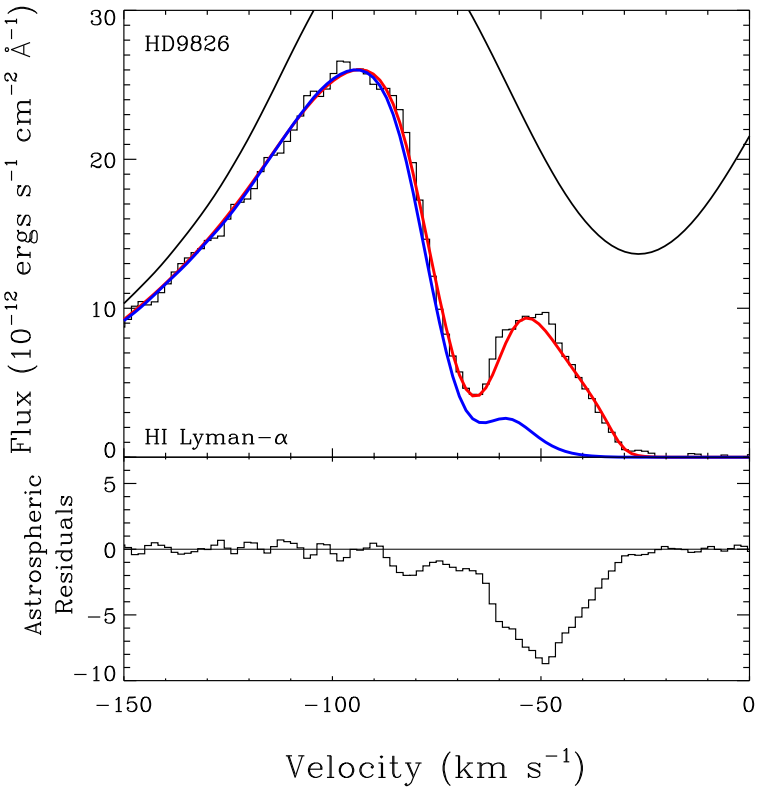

Figure 11. Same as Figure 10 but for HD 9826 with a mass-loss rate of 5.1 $\dot{M}_{\odot}$. The residuals associated with the inclusion of astrosphere absorption are centered at –50 km s^{-1}.

A second possibility for nondetection could be that the line of sight to the star is at a large angle with respect to the nose of the incoming interstellar flow. The maximum velocity difference occurs when observing at the same angle as the inflow. At a tangential angle the astrospheric velocity difference is close to zero, and when observing close to the tail (180° from the inflow direction) the absorption by the hydrogen gas flowing past the star is likely redshifted relative to the interstellar velocity (Wood et al. 2014a). Figure 9 shows plasma models for the astrospheres of HD 9826 and HD 192310, showing the location of the hydrogen walls. These simulations are multifluid, axisymmetric, hydrodynamic models treating the charge exchange of interstellar neutrals with protons in the stellar wind, originally developed for the heliosphere. The models assume that hydrogen is 42% ionized, similar to what has been determined for the LISM near the Sun. Our multifluid treatment successfully approximates the non-Maxwellian distribution of neutral hydrogen associated with the interaction of the heliosphere with the surrounding local interstellar medium. Further details regarding this type of model can be found in Zank et al. (1996), Zank (1999), Heerikhuisen et al. (2008), Müller et al. (2006), and Pogorelov et al. (2017). The observed sight lines (indicated in the figure) are 39.6° for HD 9826 and 44.7° for HD 192310, respectively, relative to the inflow nose. Table 5 provides a more detailed look at the model parameters, and Figures 10 and 11 show the expected astrospheric absorption based on these models for HD 192310 and HD 9826, respectively, assuming stellar mass loss rates of 5.9 $\dot{M}_{\odot}$ for HD 192310 and 5.1 $\dot{M}_{\odot}$ for HD 9826. These mass loss rates are based on the stellar X-ray luminosities and the correlation with mass loss identified by Wood et al. (2005b) (with a recent version in Wood et al. (2014b)). If hydrogen walls are present, they should have been detected.

The third possibility is that the stars are not located inside of interstellar clouds containing neutral hydrogen gas. The vast majority of analyzed stars of distances greater than 10 pc yield non-detections of astrospheric absorption (Wood et al. 2005b), which is likely due to stars being surrounded by ionized plasma within the Local Bubble. In this case, the hydrogen wall structure will be significantly different, if present at all (Müller et al. 2006), and thus no astrospheric signatures are expected in the Lyman-α line profiles. We believe that this is the most likely explanation for the non-detections because the low column density and favorable observing angles are both conducive for detection.

Table 5. Model Astrosphere[a] Parameters

Star Name	v(ISM) (km s^{-1})	Ionization Fraction (ISM)	n(ISM) Total (cm^{-3})	Sightline Angle (θ)	v(Stellar Wind) at 1 AU (km s^{-1})	n(Stellar Wind) at 1 AU (cm^{-3})	Stellar Mass Loss Rate ($\dot{M}_{\odot}$)
HD 9826	56.0	42%	0.24	39.9	400	25.3	5.1
HD 192310	52.0	42%	0.24	44.7	400	29.4	5.9

[a] These are axisymmetric, multifluid, hydrodynamical models that assume a temperature of 100,000 K at 1 AU for the stellar wind, and 8,000 K for the ISM. A solar wind density of 5 cm^{-3} and velocity of 400 km s^{-1} at 1 AU were used as a basis for expressing the mass loss rates of these solar-like stars.

6. CONCLUSIONS

Our analysis of the high-resolution STIS spectra of three nearby planet-hosting stars allowed us to identify and measure the properties of nine interstellar absorption components along their lines of sight. We can reliably assign eight of the nine components with interstellar clouds previously identified by Redfield & Linsky (2008) on the basis of location inside or very near the cloud boundary and radial velocity within 2.0 km s^{-1} of that predicted from the cloud's velocity vector. In all eight cases, the measured and predicted temperatures agree within the admittedly large errors and the turbulence and depletions agree in most cases.

None of the three stars show any direct evidence of astrosphere absorption, implying that these stars are likely not located inside of the partially ionized clouds observed along their lines of sight. Instead, these stars are likely surrounded by fully ionized interstellar gas that produces very different or no hydrogen walls. We cannot, therefore, estimate the mass-loss rates for these three planet-hosting stars by the astrosphere technique.

We also predict the interstellar radial velocities of clouds located along the lines of sight to all known planet-hosting stars within 20 pc of the Sun. Although our knowledge of the clouds and their kinematic properties is incomplete, the predicted velocities should prove useful in analyzing low-resolution spectra of these stars to search for weak absorption or emission from their exoplanets. Also, analysis of stellar winds using the astrosphere technique requires knowledge of the interstellar flow vector.

Alongside the kinematics, measuring the densities of various ions within the clouds is a necessary step when interpreting spectroscopic measurements commonly used in exoplanet characterization. For example, without accounting for Lyman-α absorption within the ISM along the sight line, it is impossible to accurately characterize exoplanet mass loss during and after transits by analyzing line of sight spectra.

Without careful analysis of the many features of the local interstellar medium, our picture of our local environment remains incomplete. Therefore, as our characterization and scrutiny of exoplanetary atmospheres becomes more precise over the coming decades, it will be critical to have detailed observations and knowledge of the intervening and surrounding interstellar medium.

We acknowledge support by *HST* Grants GO-12475 and GO-12596 awarded by the Space Telescope Science Institute, which is operated by the Association of Universities for Research in Astronomy, Inc., for NASA, under contract NAS 5-26555. EE gives thanks for the student fellowship awarded from the Connecticut Space Grant Consortium in support of this research.

This work has made use of data from the European Space Agency (ESA) mission *Gaia* (https://www.cosmos.esa.int/gaia), processed by the *Gaia* Data Processing and Analysis Consortium (DPAC, https://www.cosmos.esa.int/web/gaia/dpac/consortium) Funding for the DPAC has been provided by national institutions, in particular the institutions participating in the *Gaia* Multilateral Agreement.

Facility: *HST* (STIS)

REFERENCES

Asplund, M., Grevesse, N., & Sauval, A. J. 2005, Cosmic Abundances as Records of Stellar Evolution and Nucleosynthesis, 336, 25

Ayres, T. R. 2010, ApJS, 187, 149

Butler, R. P., Marcy, G. W., Williams, E., Hauser, H., & Shirts, P. 1997, ApJL, 474, L115

Butler, R. P., Marcy, G. W., Fischer, D. A., et al. 1999, ApJ, 526, 916

Curiel, S., Cantó, J., Georgiev, L., Chávez, C. E., & Poveda, A. 2011, A&A, 525, A78

Decker, R. B., Krimigis, S. M., Roelof, E. C., et al. 2008, Nature, 454, 67

Draine, B. T. 2011, Physics of the Interstellar and Intergalactic Medium by Bruce T. Draine. Princeton University Press.

Dupuy, T. J., & Kraus, A. L. 2013, Science, 341, 1492.

Echim, M. M. and Lemaire, J. and Lie-Svendsen, Ø. 2011, Surveys in Geophysics, 32, 1

Ehrenreich, D., Bourrier, V., Wheatley, P. J., et al. 2015, Nature, 522, 459

Fossati, L., Haswell, C. A., Froning, C. S., et al. 2010, ApJL, 714, L222

France, K., Linsky, J. L., Tian, F., Froning, C. S., & Roberge, A. 2012, ApJ, 750, L32

France, K., Loyd, R. O. P., Youngblood, A, et al. 2016, ApJ, 820, 89

Frisch, P. C., Redfield, S., & Slavin, J. D. 2011, ARA&A, 49, 237

Gaia Collaboration, Prusti, T., de Bruijne, J. H. J., et al. 2016, A&A, 595, A1.

Gaia Collaboration, Brown, A. G. A., Vallenari, A., et al. 2018, A&A, 616, A1.

Gauza, B., Béjar, V. J. S., Pérez-Garrido, A., et al. 2015, ApJ, 804, 96.

Gayley, K. G., Zank, G. P., Pauls, H. L., Frisch, P. C., & Welty, D. E. 1997, ApJ, 487, 259

Grünwaldt, H., Neugebauer, M., Hilchenbach, M., et al. 1997, Geophysical Research Letters, 24, 1163.

Gry, C., & Jenkins, E. B. 2014, A&A, 567, A58

Gurnett, D. A., Kurth, W. S., Burlaga, L. F., & Ness, N. F. 2013, Science, 341, 1489

Heerikhuisen, J., Pogorelov, N. V., Florinski, V., et al. 2008, ApJ, 682, 679.

Hernandez, S., et al. 2011, "STIS Instrument Handbook" Version 13.0, (Baltimore: STScI)

Howard, A. W., Johnson, J. A., Marcy, G. W., et al. 2011, ApJ, 730, 10

Jakosky, B. M., Brain, D., Chaffin, M., et al. 2018, Icarus, 315, 146.

Izmodenov, V., Malama, Y. G., Gloeckler, G., et al. 2003, ApJ, 594, L59.

Lammer, H., Chassefière, E., Karatekin, Ö., et al. 2013, SSRv, 174, 113

Lindler, D. 1999, CALSTIS Reference Guide (Greenbelt: NASA/LASP)

Linsky, J. L., Draine, B. T., Moos, H. W., et al. 2006, ApJ, 647, 1106

Linsky, J. L., Bushinsky, R., Ayres, T., & France, K. 2012, ApJ, 757, 69

Linsky, J. L., France, K., & Ayres, T. 2013, ApJ, 766, 69

Loyd, R. O. P., Koskinen, T. T., France, K., Schneider, C., & Redfield, S. 2017, ApJL, 834, L17

Luhmann, J. G. 2003, ApJ, 592, 1241

Luhman, K. L., Patten, B. M., Marengo, M., et al. 2007, ApJ, 654, 570

Malamut, C., Redfield, S. Linsky, J. L., Wood, B. E. & Ayres, T. R. 2014, ApJ, 787, 75

McComas, D. J., Alexashov, D., Bzowski, M., et al. 2012, Science, 336, 1291

Miguel, Y., Kaltenegger, L., Linsky, J. L., & Rugheimer, S. 2015, MNRAS, 446, 345

Morton, D. C. 2004, ApJS, 151, 403

Müller, H.-R., Frisch, P. C., Florinski, V., & Zank, G. P. 2006, ApJ, 647, 1491

Pepe, F., Lovis, C., Ségransan, D., et al. 2011, A&A, 534, A58

Perryman, M. A. C., Lindegren, L., Kovalevsky, J., et al. 1997, A&A, 500, 501.

Pogorelov, N. V., Heerikhuisen, J., Roytershteyn, V., et al. 2017, ApJ, 845, 9.

Redfield, S., & Linsky, J. L. 2000, ApJ, 534, 825

Redfield, S., & Linsky, J. L. 2001, ApJ, 551, 413

Redfield, S., & Linsky, J. L. 2002, ApJS, 139, 439

Redfield, S., & Linsky, J. L. 2004a, ApJ, 602, 776

Redfield, S., & Linsky, J. L. 2004b, ApJ, 613, 1004

Redfield, S., & Linsky, J. L. 2008, ApJ, 673, 283-314

Redfield, S., & Linsky, J. L. 2015, ApJ, 812, 125

Rodriguez, D. R., Zuckerman, B., Melis, C., & Song, I. 2011, ApJL, 732, L29

Scherer, K., & Fichtner, H. 2014, ApJ, 782, 25.

Slavin, J. D., & Frisch, P. C. 2008, A&A, 491, 53

Stassun, K. G., Collins, K. A., & Gaudi, B. S. 2017, AJ, 153, 136

Stone, E. C., Cummings, A. C., McDonald, F. B., et al. 2005, Science, 309, 2017

Stone, E. C., Cummings, A. C., McDonald, F. B., et al. 2008, Nature, 454, 71

van Belle, G. T., & von Braun, K. 2009, ApJ, 694, 1085.

Vidal-Madjar, A., Lecavelier des Etangs, A., Désert, J.-M., et al. 2003, Nature, 422, 143

Wood, B. E., Alexander, W. R., & Linsky, J. L. 1996, ApJ, 470, 1157

Wood, B. E., Müller, H.-R., Zank, G. P., & Linsky, J. L. 2002, ApJ, 574, 412

Wood, B. E. 2004, Living Reviews in Solar Physics, 1, 2

Wood, B. E., Müller, H.-R., Zank, G. P., Izmodenov, V. V., & Linsky, J. L. 2004, Advances in Space Research, 34, 66

Wood, B. E., Linsky, J. L., Müller, H.-R., & Zank, G. P. 2001. 2001, ApJL, 547, L49

Wood, B. E., Linsky, J. L., Hébrard, G., Williger, G. M., Moos, H. W., & Blair, W. P. 2004, ApJ, 609, 838

Wood, B. E., Redfield, S., Linsky, J. L., Müller, H.-R., & Zank, G. P. 2005, 13th Cambridge Workshop on Cool Stars, Stellar Systems and the Sun, 560, 309

Wood, B. E., Redfield, S., Linsky, J. L., Müller, H.-R., & Zank, G. P. 2005b, ApJS, 159, 118

Wood, B. E., Izmodenov, V. V., Alexashov, D. B., Redfield, S., & Edelman, E. 2014a, ApJ, 780, 108

Wood, B. E., Müller, H.-R., Redfield, S., & Edelman, E. 2014b, ApJL, 781, L33

Youngblood, A., France, K., Loyd, R. O. P., et al. 2016, ApJ, 824, 101

Zachary, J., Redfield, S., Linsky, J. L., & Wood, B. E. 2018, ApJ, 859, 42

Zank, G. P. 1999, SSRv, 89, 413

Zank, G. P., Pauls, H. L., Williams, L. L., & Hall, D. T. 1996, J. Geophys. Res., 101, 21639

Zank, G. P., Pogorelov, N. V., Heerikhuisen, J., et al. 2009, SSRv, 146, 295

Table 6. LISM Properties for the Sightlines to Planet-Hosting Stars within 20 pc of the Sun[a]

Star		d[b]	l	b	m_v	LISM[c]	Component 1		Component 2		Component 3		Ref[d]
		(pc)	(°)	(°)		clouds	v_{rad}	N(HI)	v_{rad}	N(HI)	v_{rad}	N(HI)	
Proxima Cen	GJ 551	1.30	313.94	−1.93	11.13	G	−18.1	17.6					3
Lalande 21185	GJ 411	2.55[e]	185.12	+65.43	7.52	LIC	(4.66)	(17.10)					8
ϵ Eri	GJ 144	3.20	195.85	−48.05	3.73	LIC	16.1	17.93					6
Ross 128	GJ 447	3.37	270.15	+59.56	11.15	Leo,NGP	(−0.86)		(0.13)				8
HD 1326	GJ 15A	3.56	116.68	−18.45	8.13	LIC,Hyades	(9.20)	(18.06)	(10.06)				8
τ Cet	GJ 71	3.60	173.10	−73.44	3.50	LIC	12.34	18.0					2
YZ Cet	GJ 54.1	3.71	149.71	−78.76	12.07	LIC,Mic,Cet	(9.00)	(17.99)	(4.92)		(16.75)		8
HIP 36208	GJ 273	3.80[f]	212.34	+10.37	9.87	LIC,Aur,Gem	(19.65)	(17.86)	(22.52)		(35.42)		8
Kapteyn	GJ 191	3.93	250.53	−36.00	8.85	Blue,Dor	(10.40)		(21.48)				8
Wolf 1061	GJ 628	4.31	3.35	+23.68	10.07	G,Mic	(−29.55)		(−25.15)				8
HIP 86162	GJ 687	4.55	98.60	+31.96	9.15	LIC	(−2.32)	(17.39)					8
HIP 85523	GJ 674	4.55	343.00	−6.78	9.41	G,Aql	(−24.37)		(−28.24)				8
IL Aqr	GJ 876	4.68	52.00	−59.63	10.19	LIC	2.8	18.03					6
HD 204961	GJ 832	4.97	349.17	−46.35	8.67	LIC	−17.1	18.20					6
HD 26965	GJ 166A	5.04	200.75	−38.05	4.43	LIC	21.73	17.8					2
	GJ 3323	5.38	206.43	−27.47	12.20	LIC,Aur,Hyades	(21.97)	(17.89)	(24.65)		(11.69)		8
HD 20794	GJ 139	6.00	250.75	−56.08	4.27	Dor,Blue,G	(31.42)		(9.33)		(14.87)		8
HIP 74995	GJ 581	6.30	354.08	+40.02	10.56	G,Gem	−24.1[g]	18.01[g]	(−27.57)				2,8
HIP 80459	GJ 625	6.47	83.21	+42.79	10.17	LIC,Oph,NGP	(−7.77)	(16.87)	(−16.28)		(−10.08)		8
HD 219134[h]	GJ 892	6.53	109.90	−3.20	5.57	LIC	(5.53)	(18.03)					8
HD 156384	GJ 667C	7.25	351.84	+1.42	5.89	G	−22.5	17.98					6
Fomalhaut	GJ 881	7.70[f]	20.49	−64.91	1.16	LIC,Mic	−5.87	(17.40)	−10.64				2,8
HIP 86287	GJ 686	8.16	42.24	+24.30	9.58	LIC,Mic,Oph	(−19.54)	(16.39)	(-25.11)		(-29.11)		8
61 Vir	GJ 506	8.51	311.86	+44.09	4.74	NGP,Leo	−14.74	17.9	(−11.01)				2,7
HD 192310	GJ 785	8.80	15.62	−29.40	5.72	Vel,Mic,LIC	−30.40	17.96	−24.24	17.90	−18.18	16.17	1
HIP 109388	GJ 849	8.80	55.89	−45.40	10.37	LIC	(−6.80)	(17.56)					8
HIP 56528	GJ 433	9.07	284.88	+27.65	9.81	Gem	(6.51)						8
HD 102365	GJ 442A	9.29	289.80	+20.71	4.88	G	(−10.52)						8
HD 285968	GJ 176	9.47	180.02	−17.43	9.51	LIC,Hyades,Aur	29.0[g]	17.46[g]	(12.9)		(21.71)		6,8
Ross 905[h]	GJ 436	9.76	210.54	+74.56	10.61	?	−4.1	18.04					6
WISE J1217+1626		10.10[i]	265.24	+76.80		NGP,Leo	(−1.28)		(−2.07)				8
LHS 3776	GJ 1265	10.26	39.08	−52.51	13.67	LIC	(-7.61) (17.35)						8
β Gem	GJ 286	10.36[f]	192.23	+23.41	1.14	LIC,Gem	19.65	18.0	31.84	17.8			2
HIP 83043	GJ 649	10.38	46.52	+35.34	9.66	NGP,Oph,LIC	(−26.10)		(−25.73)		(−17.78)	(16.42)	8
HD 122303	GJ 536	10.41	335.06	+55.81	9.71	NGP,Leo,Gem	(−19.89)		(−13.53)		(−13.15)		8
HD 147379	GJ 617A	10.77	99.90	+39.47	8.90	LIC	(−2.55)	(17.28)					8
HD 13445	GJ 86	10.79	275.93	−61.96	6.17	Cet,Dor,Vel	(13.44)		(26.73)		(16.78)		8
HD 57050	GJ 1148	11.02	210.34	+9.26	8.71	LIC,Aur	(20.16)	(17.89)	(22.72)				8
HD 3651	GJ 27	11.14	119.17	−41.53	5.88	LIC,Hyades	(10.24)		(12.32)				8
HD 85512	GJ 370	11.28	271.68	+8.16	7.65	G,Cet	−3.3[g]	18.43[g]	(14.3)				6,8
HIP 63510	GJ 494	11.51	311.83	+75.09	9.75	NGP	(-8.39)						8
HIP 11048	GJ 96	11.94	138.29	−12.27	9.35	LIC	(16.18)	(18.27)					8
HIP 22627	GJ 179	12.36	192.23	−22.86	12.02	LIC,Aur,Hya	(23.46)	(18.01)	(23.75)		(12.64)		8
Trappist-1[h]		12.43	69.71	−56.64	18.80	LIC,Cet	(−1.25)	(17.86)	(−12.21)				8
HD 69830	GJ 302	12.56	234.56	+12.82	5.95	LIC,Aur	(14.04)	(17.43)	(20.21)				8
55 Cnc[h]	GJ 324A	12.59	196.79	+37.70	5.95	LIC,Gem	(14.75)	(17.78)	(27.78)				8
	GJ 1132[h]	12.62	277.26	+7.76	13.52	G,Cet	(-2.73)		(8.82)				8
VHS J1256-1257		12.7[j]	304.67	+49.90	17.76	Leo	(-8.71)						8
HD 147513	GJ 9559	12.91	341.62	+7.21	5.38	G,Gem	(−26.63)		(−25.30)				8
HD 40307	GJ 2046	12.94	268.81	−30.34	7.15	Blue,G,Vel	9.4	18.60	(7.63)		(18.38)		6,8
HD 9826	GJ 61	13.41	132.00	−20.67	10.07	?,Hyades,LIC	9.11	17.78	12.14	17.55	16.45	17.34	1
γ Cep	GJ 903	13.54	118.99	+15.32	3.22	LIC	(8.33)	(18.04)					8
Ross 1020	GJ 3779	13.75	14.12	+82.43	13.01	NGP	(-8.29)						8
47 UMa	GJ 407	13.80	175.78	+63.37	5.04	LIC,NGP	(5.31)	(17.23)	(12.91)				8
	GJ 1214[h]	14.65	26.16	+23.61	14.67	Mic,G,Oph	−26.4[g]	18.06[g]	(−27.76)		(−28.78)		6,8
HIP 79431		14.54	355.20	+22.97	11.37	G,Gem	(−29.24)		(−28.63)				8
HD 136352	GJ 582	14.69	327.08	−7.38	5.65	G	(−20.49)						8
LHS 3844		14.89	318.25	−43.91		Vel	(-7.31)						8
HIP 49189	GJ 378	14.96	168.73	+51.19	10.14	LIC	(9.56)	(17.63)					8
LHS 1140[h]	GJ 3053	14.99	115.40	−78.05	14.15	LIC,Mic,Cet	(6.90)	(18.01)	(1.85)		(10.67)		8
HIP 19394	GJ 163	15.14	262.78	−45.32	11.8	Dor,G,Blue	(21.29)		(11.36)		(8.56)		8
LHS 2037	GJ 317	15.20	246.80	+11.19	11.98	G,Cet	(10.61)		(35.87)				8
HD 38858	GJ 1085	15.25	209.38	−15.84	5.97	LIC,Aur	(22.16)	(17.90)	(25.19)				8
51 Peg	GJ 882	15.47	90.06	−34.73	5.46	Eri,Hyades	(−1.23)		(8.11)				8

Table 6 continued on next page

Table 6 *(continued)*

Star		d[b]	l	b	m_v	LISM[c]	Component 1		Component 2		Component 3		Ref[d]
		(pc)	(°)	(°)		clouds	v_{rad}	N(HI)	v_{rad}	N(HI)	v_{rad}	N(HI)	
HD 160691	GJ 691	15.61	340.06	−11.50	5.15	G,Aql	(−22.64)		(−23.30)				8
τ Boo	GJ 527	15.66	358.94	+73.89	4.49	NGP,Gem	−11.64		(−9.60)				7,8
HD 190360	GJ 9683	16.01	67.41	−0.67	5.71	Mic,G,Aql	(−20.27)		(−12.49)		(−17.76)		8
HIP 85647	GJ 676A	16.03	339.10	−9.54	9.59	G,Aql	(−22.96)		(−24.75)				8
HD 113538	GJ 9425	16.29	305.03	+10.37	9.06	G	(−15.72)						8
HD 21749	GJ 143	16.33	279.23	−45.82	8.14	G,Cet,Vel	(5.88)		(12.19)		(13.98)		8
HD 128311	GJ 3860	16.34	2.73	+59.84	7.45	Gem,Leo,NGP	(−17.25)		(−14.68)		(−21.38)		8
HD 177565	GJ 744	16.93	359.45	−19.08	6.16	Aql,Vel,Mic	(−19.85)		(−36.07)		(−24.07)		8
HIP 79126	GJ 3942	16.94	82.20	+45.47	10.25	NGP	(−10.29)						8
HD 7924	GJ 9054	17.00	124.74	+13.95	7.19	LIC	(9.21)	(18.14)					8
HD 17051	GJ 108	17.33	268.81	−58.32	5.40	G,Dor,Vel	(10.31)		(26.61)		(19.53)		8
HD 10647	GJ 3109	17.34	286.90	−61.77	5.52	Dor,Vel,Cet	(23.93)		(12.70)		(8.12)		8
ρ Cor Bor	GJ 9537	17.48	53.49	+48.92	5.41	NGP,Mic,Oph	(−20.13)		(−17.32)		(−20.05)		8
HD 1237A	GJ 3021	17.56	304.87	−37.14	6.58	G,Vel,Cet	(−4.88)		(−3.14)		(−8.93)		8
ϵ Vir	GJ 504	17.54	322.79	+71.31	5.22	NGP,Leo	(−11.35)		(−8.37)				8
HD 189567	GJ 776	17.91	328.47	−31.99	6.07	G,Vel	(−13.49)		(−18.32)				8
70 Vir	GJ 9446	17.91	337.67	+74.10	4.97	NGP,Leo	(−11.89)		(−8.79)				8
14 Her	GJ 614	17.94	69.17	+46.94	6.67	NGP,Oph	(−15.36)		(−18.45)				8
HD 206860	GJ 9751	18.13	69.86	−28.27	5.95	Vel,Eri,LIC	−14.68	17.35	−8.00	17.79	−5.44	18.14	1
HIP 84460	GJ 3998	18.16	32.27	+26.15	10.83	LIC,G,Mic	(−21.27)	(16.30)	(26.60)		(−25.88)		8
83 Leo	GJ 429	18.21	259.28	+58.51	7.53	Leo,NGP	(1.45)		(3.78)				8
HD 99492	GJ 429B	18.21	259.28	+58.51	7.53	Leo,NGP	(1.45)		(3.78)				8
HD 154088	GJ 652	18.28	355.24	+7.67	6.58	G	(−28.49)						8
HD 27442	GJ 9153	18.28	270.20	−42.56	4.44	G,Vel,Cet	(8.57)		(18.67)		(18.86)		8
HD 39091	GJ 9189	18.28	292.51	−29.78	5.67	G,Vel,Cet	(−2.26)		(2.28)		(-0.33)		8
HD 154345	GJ 651	18.29	73.02	+37.66	6.74	Oph,NGP,LIC	(−20.55)		(−15.27)		(−10.80)	(16.73)	8
HD 87883		18.30	191.19	+54.54	7.55	LIC,Leo	(8.97)	(17.46)	(10.51)				8
WD 0806-661	GJ 3483	19.26	279.42	−17.57	13.70	G,Blue,Cet	(0.88)		(4.96)		(10.31)		8
HD 192263		19.65	41.87	−18.70	7.77	Eri,Aql,Mic	(−21.58)		(−36.25)		(−26.85)		8
β Pic	GJ 219	19.75	258.36	−30.61	3.86	Blue,G	(9.32)		(11.93)				8
HD 189733[h]	GJ 4130	19.78	60.96	−3.92	7.65	Aql,Eri, Mic	(−18.64)		(−15.90)		(−22.23)		8
7 CMa	GJ 9214	19.82	228.69	−11.80	3.91	LIC,Blue	(18.08)	(17.68)	(12.66)				8

[a] Data in parentheses are predicted from models. The velocities from Redfield & Linsky (2008): http://lism.wesleyan.edu/LISMdynamics.html and column densities from Redfield & Linsky (2000): http://lism.wesleyan.edu/ColoradoLIC.html.

[b] **Distances are from GAIA DR2 (Gaia Collaboration et al. 2016, 2018) unless otherwise noted.**

[c] Interstellar partially ionized clouds in the line of sight to the star. For lines of sight with predicted interstellar velocities, the first listed cloud is predicted to be the dominant absorber.

[d] (1) This paper, (2) Redfield & Linsky (2008), (3) Wood et al. (2001), (4) Wood et al. (2014a), (5) Wood et al. (2014b), (6) Youngblood et al. (2016), (7) Malamut et al. (2014), (8) velocities from http://lism.wesleyan.edu/LISMdynamics.html and column densities from http://lism.wesleyan.edu/ColoradoLIC.html.

[e] van Belle, & von Braun (2009)

[f] Perryman et al. (1997)

[g] N(H I), actually log N(H I), is the sum of all velocity components, and v_{rad} is the measured mean velocity when several velocity components are likely present in this line of sight.

[h] Hosts a transiting exoplanet.

[i] Dupuy, & Kraus (2013)

[j] Gauza et al. (2015)